# Modeling the Transmission of Optical Lightning Signals through Complex Three-Dimensional Cloud Scenes

**Michael Peterson**[1]

[1] ISR-2, Los Alamos National Laboratory, Los Alamos, New Mexico

Corresponding author: Michael Peterson (mpeterson@lanl.gov), B241, P.O. Box 1663 Los Alamos, NM, 87545

**Key Points:**

- Lightning measurements from space have revealed complex interactions between optical emissions and nearby clouds
- Monte Carlo radiative transfer simulations are conducted to examine how complex cloud scenes are illuminated by lightning
- Modeling results support the suggested origins of irregular spatial radiance patterns and unobscured lightning producing "superbolts"

LA-UR 20-23479

## Abstract

Space-based lightning imagers have shown that complex cloud scenes that consist of multiple tall convective features, anvil clouds, and warm boundary cloud layers are illuminated by lightning in many different ways, depending on where the lightning occurs and how energetic it is. Modifications to the optical lightning signals from radiative transfer in the cloud medium can lead to reductions in detection efficiency and location accuracy for these instruments, and can also cause some of the optical signals that are detected to have unexpected spatial energy distributions. In this study, we perform Monte Carlo radiative transfer simulations of optical lightning emissions in clouds with complex three-dimensional geometries to shed some light on the origins of certain irregular radiance patterns that have been recorded from orbit. We show that reflections off nearby cloud faces can explain lightning signals in non-electrified clouds, tall clouds can result in poor optical transmission and suppressed radiances that could lead to missed events, and that particularly favorable viewing conditions can cause otherwise normal lightning to produce a "superbolt" that is orders of magnitude brighter than the same flash seen from a different direction.

## Plain Language Summary

Lightning is detected from space using instruments that report rapid changes in cloud brightness from lightning illumination. However, this light can be modified by scattering and absorption in the cloud. Scattering off water drops causes portions of the signal to be diluted in space and delayed in time. What starts off as point impulsive light source in the cloud may illuminate a region of the cloud-top 100 km across with a waveform that lasts a significant fraction of a millisecond.

Interactions between the optical lightning emissions and the cloud scene are particularly complex when the surrounding clouds do not take on a simple geometric shape. Clouds observed in nature often contain multiple vertical layers including warm boundary clouds and overhanging anvils. Understanding some of the more irregular spatial energy distributions recorded by space-based lightning sensors requires accounting for these complex geometries.

In this study, we develop 3D cloud models that approximate cloud structures found in nature, and perform Monte Carlo radiative transfer simulations of how they are illuminated by lightning. In doing so, we confirm the suspected origins of irregular cloud illumination, such as reflections off of nearby cloud faces or particularly-favorable viewing conditions allowing normal lightning to appear highly-energetic.

## 1 Introduction

Pixelated lightning imagers including the Lightning Imaging Sensor (LIS: Christian et al., 2000; Blakeslee et al., 2014) and Geostationary Lightning Mapper (GLM: Goodman et al., 2013; Rudlosky et al., 2019) record the spatial distributions of optical energy that result from lightning pulses. These observed spatial radiance patterns often deviate from the simple idealized model of radiance decreasing only with radius from the center pixel. We previously reported cases of highly-irregular radiance patterns where the shape of the optical pulse on the CCD imaging array followed the cloud boundaries (i.e., Figures 3 an 4 in Peterson et al., 2017a), cases where the radiance pattern extended outward from the edge of the thunderstorm core giving an incorrect impression that these warm boundary clouds were producing lightning (Peterson et al., 2017b), and cases where optical emissions were blocked from reaching orbit by certain cloud regions, resulting in "holes" in otherwise-contiguous flash footprints (i.e., Figure 1 in Peterson and Liu, 2013). Unobscured lightning sources have also been proposed as the mechanism responsible for certain lightning "superbolts" (Turman, 1977) that primarily illuminate the edge of the storm (Peterson et al., 2020).

Irregularities in lightning radiance patterns result from interactions between the optical lightning emissions and complex cloud scenes. Clouds modify optical lightning signals through absorption and scattering. While absorption prevents photons from reaching the space-based instrument entirely, multiple scattering diverts the photons from the direct path to the instrument. Some light will be redirected away from the sensor, while the signals that do arrive are broadened in space and diluted in time according to the path they took through the cloud. As clouds are invisible to Radio-Frequency (RF) signals, coordinated optical and RF measurements

have been used to quantify the severity of scattering delays (Suszcynsky et al., 2000; Light et al., 2001a) and to demonstrate reduced detection capabilities for optical space-based imagers when sources occur at low-altitudes in the cloud (Thomas et al., 2000).

Computational models have been employed to gain insights into how clouds modify optical lightning emissions. Thomson and Krider (1982) developed a Monte Carlo method for simulating optical transmission of transient light sources (both point sources and extended sources) through three-dimensional clouds of various geometries (cubic, spherical, and cylindrical). By measuring the path lengths taken by the emitted photons, they were able to further comment on typical scattering delays in the optical signals. Koshak et al. (1984) leveraged one-speed Boltzmann transport theory with diffusion approximations (essentially, treating the thundercloud as a nuclear reactor and replacing neutrons with photons) to model the waveforms that would be recorded from a high-altitude aircraft (or spacecraft) from spatially-complex lightning sources after scattering through homogeneous rectangular parallelepiped clouds. Light et al. (2001b) took a similar Monte Carlo approach to Thomson and Krider (1982), but, similar to Koshak et al. (1994), focused on the waveforms that would be measured by on-orbit sensors. Key to the present study, Light et al. (2001b) concluded that the shape of the cloud and position of the lightning event in the cloud (rather than the extent or motion of the source) are the primary factors that determine the distribution of photons escaping to space.

The primary limitation to these previous studies is that they represent homogeneous clouds with simple geometric shapes. Brunner and Bitzer (2020) used Weather Research and Forecasting (WRF) simulations of thunderstorms in a cubic model geometry to improve on how clouds were represented in Monte Carlo lightning illumination simulations by permitting inhomogeneous scattering media. However, they did not consider variations in cloud geometry,

and only reported the percentages of photons that escaped the upper cloud boundary – not how those photons were distributed across that boundary and would be imaged.

While a cylinder or even box geometry might approximate the structure of an isolated growing convective cloud, the cloud scenes monitored by LIS and GLM for lightning activity often consist of multiple convective cells with overhanging anvils that are also surrounded by warm boundary clouds. The simplistic clouds in these former model simulations are not sufficient to describe the complex interactions between the lightning emissions and the cloud scenes where we observe the irregular radiance patterns noted previously. The need for capturing complex cloud geometries was recognized by Light et al. (2001b) who stated "the most realistic [cloud] shape would be some superposition of cylindrical and planar."

In this study, we ascertain which scenarios of lightning illuminating complex three-dimensional cloud scenes lead to the irregular radiance patterns that have been noted from orbit. We construct complex three-dimensional cloud shapes using composites of cylindrical and planar geometries to approximate cloud structures found in nature. These clouds are input into optical Monte Carlo radiative transfer simulations that yield spatial radiance measurements from a detector above the thunderstorm in physical units. By varying the optical thickness of the cloud layer and moving the lightning source around the three-dimensional scene, we are able to construct artificial radiance patterns that resemble the irregular features measured from orbit – including instances of reflections off neighboring clouds, poor transmission leading to holes in the image, and unobscured sources from normal lightning producing superbolts.

## 2 Data and Methodology

In this study, we use the Monte Carlo Atmospheric Radiative Transfer Simulator (MCARaTS: Iwabuchi, 2006; Iwabuchi and Okamura, 2017) to quantify the radiance that would be measured above the thunderstorm scene from an optical point source that approximates a lightning discharge. MCARaTS is a full three-dimensional radiative transfer simulator that uses a foreword-propagating Monte Carlo photon transport algorithm to trace the trajectories of photon packets as they make their way across the scene until they are either absorbed or leave the atmosphere. The algorithm is capable of reproducing realistic 3-D effects including complex shadows and cloud side illumination (Iwabuchi, 2006). It is also adaptable for simulating a variety of optical and infrared sources including solar, thermal emission, and localized point sources.

MCARaTS inputs include models for the atmosphere and surface, and the simulation configuration that defines the properties of any light sources and imagers. In Section 2.1, we will detail the atmospheric models that we develop to represent complex cloud geometries. In Section 2.2, we will describe the remaining general MCARaTS inputs. These inputs will also be summarized for quick reference in Table 1, below. Finally, in Section 2.3, we will describe the experimental configurations that will be used to examine variations in the optical radiance patterns produced by lightning.

### 2.1 Atmospheric Models with Complex Cloud Geometries

We consider five different cloud geometries that otherwise have identical vertical extents, compositions, and optical properties. To explore the dynamics of cloud geometry on measured lightning radiance, only the 3D extent of the cloud varies between cloud types. As with Light et

al., (2001b), we assume that each cloud consists of spherical water droplets evenly distributed throughout the cloud volume. Our cloud models will nominally be based on non-frontal water clouds whose drops have an effective radius of 10 μm. The following sections describe the optical properties of these clouds as well as their 3D structure.

### 2.1.1 Scattering phase functions

Since we are concerned with cloud modifications to optical lightning signals, we assume that absorption and scattering takes place exclusively in the cloud layer. Photons in the free atmosphere will not be deflected from the forward direction or absorbed by atmospheric constituent gasses. Within the cloud layer, we assume that the phase functions for scattering interactions follow the Henyey-Greenstein approximation (van de Hulst, 1980) to the solution of the Mie scattering equations (Bohren and Huffman, 1983) below:

$$p(\mu) = \frac{1 - g^2}{(1 + g^2 - 2g\mu)^{3/2}}$$

where $\mu = cos\ \alpha$, $\alpha$ is the deflection angle relative to foreword transport, and $g$ is the asymmetry parameter for the cloud particles in question at the specified wavelength of the simulation.

Thomson and Krider (1982) specified an asymmetry factor of 0.84 for 10 μm water clouds illuminated by a near infrared (870 nm) source, while Light et al. (2001b) maintained this value for red photons. For consistency with past work, we will do the same. MCARaTS requires phase functions to be specified as arrays of angle bins from 0º to 180º. For our simulations, we specify the Henyey-Greenstein solution with $g = 0.84$ at an angular resolution of 1º per bin.

### 2.1.2 Atmospheric model

Atmospheric radiative transfer parameters are specified as 1D vertical profiles with perturbations listed on a 3D nested grid. Our models consist of 47 vertical layers that begin at the surface (0 km) and end at 30 km altitude. Within the lowest 10 km of the model domain, the layers are specified with a 250 m vertical resolution. Starting at 10 km, the layer spacing increases to 1 km. The final layers three are specified at a 10 km interval.

The 3D grid extends from the third vertical level (500 m) to the 24$^{th}$ vertical level (5750 m). In each of these 3D layers, the horizontal grid is specified as a 60x60 element array. The horizontal resolution is defined in the model configuration. Nominally, we use a 200 m horizontal resolution, resulting in cloud scenes that are 12 km across. MCARaTS imposes a cyclic boundary condition for the 3D model (Iwabuchi, 2006), meaning that clouds and local sources within the model domain are infinitely tiled horizontally. This facilitates simulations of side illumination in neighboring clouds, for example from sources located at the cloud edge.

Since we are dealing with optical sources (rather than thermal sources), the three important parameters for our simulations are the phase function ($p$) to be applied, the single scattering albedo ($\overline{\omega}_o$), and the extinction coefficient ($\sigma$). Each 1D layer and 3D gridpoint is assigned one of two states (within the cloud, or in the free atmosphere), and representative values for each of these parameters are prescribed based on this state. Inside the cloud, the Henyey-Greenstein phase function defined in the previous section is applied for $p$, and 0.99996 is selected for $\overline{\omega}_o$, again based on values from Thomson and Krider (1982) for 10 μm water clouds illuminated by a near infrared source.

The extinction coefficient depends on the density and liquid water content of the clouds in question, and also determines the optical depth ($\tau$) of the cloud. Light et al. (2001b)

194 constructed artificial drop size distributions by generating Gaussian functions centered on 10 μm,
195 and then used these drop size distributions to calculate the photon mean free path between
196 collisions with the spherical water drops. They noted that these drop size distributions are not
197 realistic, but rather were selected to facilitate computations.

198 In this study, we instead take an observational approach to determine cloud extinction
199 coefficients and optical depths. Plat (1997) parameterized aircraft observations of optical cloud
200 characteristics according to effective drop size, water content, and atmospheric forcing. In their
201 Figure 5, optical extinction coefficients are plotted for non-frontal water clouds based on
202 measurements from Stephens et al. (1978). The observed extinction coefficients ranged from >
203 0.01 $m^{-1}$ to < 0.08 $m^{-1}$, while the parameterization for clouds with $r_e = 10\ \mu m$ drops bisects
204 these aircraft data.

205 These values provide a reasonable range of extinction coefficients to consider in the
206 present study. Light et al. (2001b) and Thomson and Krider (1982) noted that typical cloud
207 optical depths vary from 80 to 400, and thus have been simulated in the literature. An optical
208 depth of 80 (400) corresponds to a cloud extinction coefficient of 0.015 $m^{-1}$ (0.076 $m^{-1}$) for a slab
209 cloud in our 3D model geometry, thus filling the range of measured values from the aircraft data
210 presented in Plat (1997). We simulate clouds with extinction coefficients throughout this range.
211 The 1D $\sigma$ profiles are specified as constant null values, while 3D $\sigma$ perturbations are assigned
212 constant values from this range (based on the experimental configuration) only in gridpoints
213 within the cloud. Extinction coefficient perturbations in the 3D model domain outside of the
214 cloud are assigned $10^{-35}$ $m^{-1}$ (a minimum value corresponding to the numerical fill value in the
215 simulation) due to constraints in the computational model.

### 2.1.3 Complex 3D Cloud Geometries

Five unique cloud types are constructed to account for finite / infinite geometries and the presence / absence of horizontal cloud layers at the top and bottom of the storm. The first cloud type is a simple infinite slab cloud. Such a cloud might stand in for stratiform clouds that are horizontally-expansive beyond the spatial scale of illumination from optical lightning pulses. The remaining four cloud types are represented as cylinders at the center of the 3D grid that fill all of its vertical layers. Images of these different cylinders are shown in Figure 1 using a wide-angle (180º FOV) camera located in the mid-levels of the 3D cloud model and pointed towards the horizon. The cylinders are illuminated from below the cloud base in Figure 1, while the camera response is normalized on a logarithmic scale to emphasize less-intense portions of the image.

The radius of these cylinders is set to 15 gridpoints (3000 m at the 200 m horizontal grid resolution). The default case ("Cylinder" in Figure 1a) lacks additional surfaces for scattering or reflections. In Figure 1b and d, a "base" cloud layer is added at the bottom of the cylinder. This base layer fills the bottom 4 vertical levels of the 3D model and has an infinite horizontal planar geometry. In Figure 1c and d, an "anvil" layer is added at the top of the cylinder. This anvil layer fills the top 5 vertical levels of the 3D model and has a cylindrical geometry with a radius of 22 gridpoints (4400 m at the 200 m horizontal grid resolution).

## 2.2 Global MCARaTS inputs

The global inputs to MCARaTS – the source, surface, and imager – are specified below. While MCARaTS allows localized sources within the atmospheric model domain, it is not capable of simulating a fully-spherical isotropic source. To overcome this limitation, we model lightning emissions using two superimposed sources: one upward-facing point source, and one

downward-facing point source. We consider these light sources to be monochromatic near-infrared sources at 870 nm following Thomson and Krider (1982). These sources are assigned an optical power of $10^9$ W, consistent with the order of magnitude in optical output from return strokes (i.e., Guo and Krider, 1982).

While surface reflections are not a focus of this study, we keep the stock seawater surface model that is included in the MCARaTS package. In Figure 1a, for example, a reflection off the surface can be noted below the cloud base. These surface reflections are only a second-order effect in our experiments. Except for the visualizations in Figure 1, all simulations place the imager at the top of the model domain (30 km) directly above the cloud center with nadir pointing. The imager records the radiance of each pixel across its Field of View (FOV). At the 200 m horizontal grid spacing, a 45º full width FOV extends slightly beyond the edge of the horizontal model domain for the 3D cloud directly below the imager. For runs with a broader FOV or more compact clouds, we can image multiple clouds at different off-boresight angles.

### 2.3 Experimental configurations

Simulations are run to support three separate MCARaTS experiments. The model setup in these experiments is depicted in Figure 2. The source is shown as a double triangle symbol (representing the upward- and downward-directed sources), while the cylinder clouds directly below the imager are superimposed and outlined. The solid line shows the overall shape of the most-complex cloud type (Cylinder + Base & Anvil), and the dashed vertical lines show the edges of the primary cylinder cloud. These clouds shapes are repeated horizontally in all directions following the cyclic boundary conditions of the model.

259 There are two possible scenarios for the horizontal source location in each experiment. In
260 Scenario A (Figure 2a), the source is placed at the geometric center of the cloud. In Scenario B
261 (Figure 2b), the source is located near the edge of the inner cylinder. The position of the source
262 in Scenario B is 1.8 grid points from the edge of the primary cylinder cloud (i.e., 360 m from the
263 cylinder edge at the 200 m horizontal model resolution). The experiments / scenarios may be
264 abbreviated by combining their designations (i.e., Experiment 2a or Experiment 3b).

265 The first experiment (Section 3.1) examines how the radiance patterns recorded by the
266 imager above the cloud change for each cloud type according to the chosen cloud extinction
267 coefficient and optical depth. In this experiment, we place the lightning source at the surface (z =
268 0 m) directly below the center of the cloud (Scenario A), and then record the radiance that is
269 detected by the imager at 30 km altitude directly above the source. Experiment 1b is not
270 performed.

271 The second experiment (Section 3.2) chooses an optical extinction coefficient from the
272 first experiment to represent thick clouds, and then examines how the radiance patterns vary with
273 (1) source altitude, and (2) source horizontal position. The source is free to move up and down
274 the dotted vertical lines in Figure 2 between 0 km and 6 km altitude with a vertical step of 100
275 m.

276 The third experiment (Section 3.3) leverages the tiled nature of the 3D model domain to
277 examine how the radiance patterns vary with off-boresight angle relative to the nadir-pointing
278 imager. The imager FOV is increased to a full width of 120º while the horizontal grid spacing of
279 the 3D cloud model is reduced to 100 m between grid cells. This allows us to compare the

radiance from multiple clouds illuminated by identical lightning sources at various points across the instrument FOV when the source is located at either the center or the edge of the storm core.

## 3 Results

### *3.1 Experiment 1: Radiance variations with cloud extinction coefficient and optical depth*

In the first experiment, we place our $10^9$ W optical source below the cloud base at the geometric center of the storm and record the radiance patterns that result from simulations with different cloud extinction coefficients. This changes the optical depth of the cloud region that optical energy must transit to reach the imager. However, while it is expected that the central cylinder or slab will permit less energy from reaching orbit as the maximum optical depth of the scene increases, interactions with cloud edges and the base layer or anvil (if present) might enable photons to take shortcut paths to the imager. This would change how the flash appears from above, even though the brightness and position of the source and the geometric structure of the cloud remain unchanged.

Figure 3 shows how the recorded radiance from the imager pixel co-located with the source (solid lines) and the brightest pixel across the scene (dashed lines) vary with the prescribed cloud extinction coefficient for each of our cloud geometries. The received radiance from the center of the cloud decreases from ~1 $Wm^{-2}sr^{-1}$ at an optical depth of 80 to ~0.003 $Wm^{-2}sr^{-1}$ at an optical depth of 400. Only slight differences can be noted between the cylindrical cloud types, while the slab geometry is slightly brighter than the other clouds at optical depths below ~250.

Because the model reports monochromatic radiance in physical units, we can put these values into perspective by comparing them with past observations of natural lightning. Christian and Goodman (1987) measured lightning from a high-altitude aircraft and reported peak radiances per flash over a range from < ~0.02 $Wm^{-2}sr^{-1}$ to 0.3 $Wm^{-2}sr^{-1}$ and radiances from all pulses that extend down to < 0.005 $Wm^{-2}sr^{-1}$. While key differences exist between these observations and our model in terms of source power (they estimated a median of $10^8$ W, a factor

of 10 less than our model source), source altitude / extent, and cloud height, it is promising that the model radiances have a similar numerical range compared to these observations.

However, the center pixel directly over the source is only the brightest pixel in the scene when the cylindrical clouds have small optical depths. At optical depths around 200-250 (depending on cloud geometry), the dashed curves in Figure 2 show the scene maximum radiance diverge from the solid curves that denote the source pixel radiance. By optical depths of 400, the brightest pixels in the scene are an order of magnitude more radiant than the pixel directly over the source. Note that this does not occur with slab geometry clouds, where the source pixel remains the brightest point in the image at large optical depths.

To demonstrate why this is occurring, Figures 4 and 5 depict the radiance patterns produced by each cloud type for runs corresponding to an optical depth of 160 (Figure 4) and 320 (Figure 5). The first five panels plot the radiance across the 3D model domain in imager pixel coordinates with the cloud type in question named in the plot title. Radiances are normalized according to the brightest pixel in each image. Dashed circles are drawn to show the diameters of the primary cylindrical cloud (at its base) and the cylindrical anvil cloud (where present). The geometric center of the cloud is indicated with asterisk symbols. The final sixth panel shows normalized radiance cross sections through the center of each image along the X axis. These cross sections are also indicated in the first five panels with horizontal dashed lines.

The clouds with the lower optical depths (Figure 4) are all brightest over the source and have radiance patterns that decrease radially with similar Gaussian curves out to near the edge of the primary cylindrical cloud (Figure 4f). The spatial radiance distributions diverge starting at this radius according to cloud geometry. While the cylindrical cloud (Figure 4b) drops

329 immediately to the model noise floor, clouds with a planar base (Figure 4c and e) have a
330 secondary peak at the maximum cloud radius. If an overhanging anvil is present (Figure 4d and
331 e), it can block radiance from reaching the imager, but illumination along its edges still
332 contributes to the secondary radiance peak.

333 These radiance patterns change as we increase the cloud extinction coefficient and optical
334 depth. The clouds in Figure 5 with maximum optical depths of 400 produce radiance peaks
335 (Figure 5f) in the same locations as the previous cloud (Figure 4f), but the cloud edges are
336 brighter than the central peak in all clouds with cylindrical geometries.

337 Here, we see the basis for holes in the lightning radiance patterns observed from space. If
338 the radiance of these central pixels falls below the minimum sensitivity of the instrument, then it
339 will only resolve the bright ring around the edge of the cloud. Figure 5c is particularly illustrative
340 of what such a radiance pattern would look like in the lightning imager measurements. Pixels
341 that correspond to shortcuts that the photons can take to avoid transmitting through the full
342 optical depth of cloud will light up while the storm core remains dark. The implication of this is
343 that poorly-transmissive clouds not only reduce the detection efficiency of the instrument, but
344 also the location accuracy – as the pixels at the edge of the cloud are considered to have
345 produced the optical impulse in question, when the source was actually located within the
346 thunderstorm core.

347

348 *3.2 Experiment 2: Radiance variations from source altitude*

349 In the second experiment, we place our point source at various locations with each cloud
350 geometry and then compare the radiance patterns recorded by the imager in each case. Figure 6a-

e compares the radiance from the pixel corresponding to the source location (solid lines) and the maximum scene radiance (dashed lines) in two scenarios for the horizontal source position: the source located at the geometric center of the cloud (Scenario A, black lines), and the source located near the edge of the primary cylindrical cloud (Scenario B, blue lines). Radiances are normalized relative to an unobscured source located at the cloud top. Figure 6f, then, computes the half width of half maximum (HWHM) in the resulting radiance pattern at each altitude and cloud type starting at 1500 m.

The radiance-altitude profiles show that the most rapid change in scene radiance occurs within the top 1 km of the cloud medium. When the source is located near the cloud top, the peak radiance is co-located with the source. Moreover, comparing the Experiment 2a curves (black) with the Experiment 2b curves (blue) suggests that this does not depend on the horizontal position of the source in the cloud. High-level sources behave as though they were embedded in slab clouds while their increased pixel radiances from having concentrated optical energies (Figure 6f) less diluted by the cloud medium provide a detection advantage over lower sources with the same optical power.

As the source is moved lower in the cloud, the curves for all finite cylindrical cloud geometries (Figure 6b-e) eventually separate. First, Scenario A begins to produce greater radiances than Scenario B, indicating additional energy loss from the instrument field of view when sources are placed near the edge of the scattering medium. Then, at a lower altitude, the source pixel loses its distinction as the brightest location in the scene. The altitudes where these separations occur, and the specific behavior of the Scenario B curves depend on the geometry of the cloud.

For Scenario A runs where the source is located at the geometric center of the cloud, the

scene maximum radiance curves separate from the source pixel radiance curves at ~2 km. Figure 7 shows the radiance patterns from 2 km sources in each cloud type (Figure 7a-e) and a cross section through the center of the scene (Figure 7f) following the convention of Figures 4 and 5. While the central peak co-located with the source is still prominent, illumination of the cloud edges has become a significant feature in the spatial radiance distributions. By this altitude, the outer peak rivals the intensity of the central peak in clouds that have a base layer (Figure 7c and e). Moving the source further downward will eventually result in the radiance patterns from Figure 5 with the center peak almost completely eroded by the cloud optical depth.

The altitudes where the outer peak overtakes the central peak is particularly prevalent in the HWHM curves in Figure 6f. HWHM increases as sources are moved away from the cloud top. For sources above the cloud, this is due to reflections off the uppermost cloud boundary. For sources within the cloud, this is due to increased scattering interactions. Mid-level sources (i.e., ~3 km altitude) have their radiant energy diluted over a large area though scattering, and this causes both a severe reduction in the maximum pixel radiance (only ~0.01% of an unobscured source) and large HWHM values (off-boresight angles of ~5° for our imager configuration and measurement geometry). However, when the outer peak becomes more radiant than the inner peak, the HWHM value suddenly increases because the HWHM algorithm is looking for the half maximum at radii beyond the peak radiance location. Ordered from highest to lowest altitude, this jump occurs first in Cylinder + Base clouds, then Cylinder + Base & Anvil clouds, then Cylinder clouds, and finally Cylinder + Anvil clouds. It does not occur with slab clouds. Thus, the presence of base cloud layers increases the altitude at which the cloud-edge peak overtakes the source pixel peak while anvils reduce this altitude.

While the Scenario B curves (blue lines) are less radiant than the Scenario A curves

(black) for sources near the tops of all cylindrical cloud geometries, radiances from low- to mid-level sources are greater in Scenario B. Reflections across the complex cloud scene are particularly important for these lower-altitude edge sources where reflective surfaces can allow the photons to take shortcuts to the imager.

Figure 8 demonstrates the role of reflections in the radiance patterns from offset lightning sources. In this case, the source is placed at 3.8 km altitude near the point where the blue curves separate in Figure 6b-e. Due to the cyclic nature of the 3D model domain, clouds and localized sources are repeated horizontally. Thus, the right side of the cloud is primarily illuminated by the visible source, while the left side of the cloud is primarily illuminated by the source in the next tile to the left (outside of the instrument FOV). For the slab cloud (Figure 8a), the radiance pattern is only influenced by the visible source. The radiance cross section (black line in Figure 8f) decreases from the source location and remains near 0% at X pixels below 100.

While the finite cylindrical clouds have a radiance peak over the source, their radiance patterns and cross sections are irregular compared to the slab cloud case. For a simple cylindrical cloud (Figure 8b), the radiance peak over the source is bounded by the cloud edge, causing the cross section (Figure 8f) to be sharper on its right side. The radiance does not reach a minimum value immediately outside of the cloud because some radiance is reflected by the ocean surface, while a second prominent peak is visible along the left side of the cloud from radiance reflecting off the cloud face to reach the imager.

Adding a base cloud layer (Figure 8c) provides a more effective reflective surface for directing the lightning emissions towards the imager. The reflection off top of the base layer is more radiant than the primary peak co-located with the source (where the photons still must transit a relatively thick cloud layer to reach the imager). The neighboring point source still

420 illuminates the west edge of the cylindrical cloud, resulting in a total of three peaks in the X
421 cross section in Figure 8f.

422 If we, instead, add an anvil to the top of the cylindrical cloud (Figure 8d), then the
423 radiance peak over the source is not shifted as notably inward as in Figure 8b (though, the same
424 effect applies at the edge of the wider anvil cloud). This case also results in three peaks in the
425 radiance cross section in Figure 8f: the source peak, the right edge of the anvil cloud near the
426 source, and the left edge of the anvil cloud reflecting radiance from the next source over. These
427 latter two peaks are not as bright as the source peak.

428 Finally, if we add both a lower base layer and an upper anvil cloud to the simple cylinder
429 cloud, the radiance pattern (Figure 8e) combines all of these effects. The source peak is nearly as
430 radiant as in the anvil-only case (brighter than either the simple cylinder or base layer only
431 geometries). However, while the anvil cloud blocks much of the radiance that reflects off of the
432 lower base layer from reaching the imager, the second peak at the anvil cloud edge produces the
433 strongest radiance in Figure 8f aside from the slab cloud source peak.

434 These radiance patterns show that increasing the complexity of the cloud scene provides
435 more opportunities for the radiance pattern to diverge from the Gaussian spatial radiance
436 distributions seen in slab clouds – especially when sources are offset from the geometric center
437 of the cloud. The distinct variations between the radiance patterns from each cloud geometry
438 discussed above further supports the idea that we can make inferences about cloud geometry and
439 structure based on how the clouds are illuminated by lightning.

440

441 *3.3 Experiment 3: Radiance variations from look angle*

442 The first two experiments consider how clouds directly below the imager are illuminated

443 by lightning sources. In the third experiment, we expand the imager FOV while decreasing the
444 horizontal grid spacing of the cloud model to image multiple clouds illuminated by surface-level
445 sources at various points across the scene.

446 Radiance patterns from Scenario A (centered lightning source) are shown in Figure 9 for
447 each of our cloud geometries. Because the imager has a square shape with each axis (X and Y)
448 covering 120°, the corner pixels (outside of the inner dashed circle) extend out beyond this
449 nominal angular FOV. The horizon below the camera (~75° from nadir) can be noted in the
450 corners of the image (outer dashed line) where the illuminated clouds seem to disappear from the
451 image. Each of the images in Figure 9a-e are normalized relative to the brightest pixel in the
452 image, as before. However, instead of a cross section through the center of the image, the final
453 panel (Figure 9f) shows the peak radiance in each ring corresponding to a particular off-boresight
454 angle.

455 A common feature for all finite cylindrical cloud types (Figure 9b-e) is that the center
456 cloud that we examined in Experiments 1 and 2 is the least radiant cloud in the scene. Clouds
457 that are not located at nadir provide more shortcut paths that photons can take to the imager. As a
458 result, less of the radiance is diluted or extinguished from the instrument FOV. The radial
459 distribution of peak radiance (Figure 9f) is similar for all cloud types for the first three peaks (up
460 to ~45°). Within this range, the peak radiance from all cloud tiles (except the cloud at nadir) is
461 approximately the same and does not notably increase with the off-boresight angle of the cloud
462 in question.

463 However, not all cloud tiles in the image achieve these peak radiance values. Particularly
464 along the central X and Y axes in Figure 9b-e (pixel coordinate 400), the clouds near the edge of
465 the nominal X and Y FOV (60°) have their radiance blocked by the top of the neighboring cloud

466 closer to the center of the image. This blocking is especially important for cloud types with anvil
467 layers (Figure 9d and e) because the cylindrical anvils at the cloud top have an increased
468 diameter compared to the primary cylindrical cloud.

469 These competing factors – the relative visibility of the source and blocking by
470 neighboring clouds – cause the angular peak radiance distributions for each cloud type to diverge
471 at off-boresight angles beyond 45°. The key factor for how the radiance distributions behave
472 after this point is whether the cloud geometry has a base layer. If no base layer is present, then
473 the peak radiance begins to increase with off-boresight angle, as the source is less obscured when
474 the cloud is viewed form the side. Anvil clouds (if present) are more effective at blocking
475 radiance at large off-boresight angles than narrow cylinders. Thus, the Cylinder cloud type (blue
476 line in Figure 9f) reaches a maximum peak radiance between the nominal (60°) and overall (75°)
477 edge of the imager FOV that is 4x brighter than any other cloud type, while the Cylinder + Anvil
478 cloud type (red line) angular peak radiance distribution decreases.

479 If a base layer is present, however, then the angular peak radiance distributions do not
480 notably increase beyond off-boresight angles of 45°. The various peaks in these distributions
481 (corresponding to unique cloud tiles) maintain their off-nadir values from angles < 45°. It should
482 be noted that these trends are only valid for the cloud tile spacing and measurement geometry
483 considered by these simulations. Radiance certainly changes significantly with off-boresight
484 angle when the imager is located at higher altitudes.

485 Figure 10 depicts the radiance patterns that result from Scenario B where the source is
486 placed near the (right) edge of the primary cylindrical cloud. Blocking by neighboring clouds is
487 particularly important when the source is located at the edge of the storm. Tiles where entire
488 cloud volumes separate the source from the imager remain dark – including most of the right side

of the imager FOV and also sources along the central X axis at pixel coordinates < 200. However, this blocking is not evident in Figure 10b and d because it is overshadowed by extremely-bright pixels in the tiles to the left of center. These pixels have a direct sight line on the lightning source. When the base layer is present, it dilutes the optical emissions from the offset source, causing the peak radiance profiles for the Cylinder + Base and Cylinder + Base & Anvil cloud geometries in Figure 10f to behave in a similar manner to the slab cloud geometry (black curve) – only at a greater radiance due to its thin vertical extent. Without this base layer, the Cylinder and Cylinder + Anvil cloud geometries record the unimpeded radiance from the source. Indeed, the maximum values in their angular peak radiance distributions (blue and red curves) nearly reach 100% of the radiance of the unobstructed cloud-top source.

We are, essentially, describing the conditions that allow ordinary lightning to be measured as a "superbolt." Having this direct unobscured line on the source can cause the peak radiance to be 5 orders of magnitude brighter than the same exact source below a cloud layer – either on the edge of the storm but below a base layer of warm cloud, or centered in the storm core (Figure 9). Since superbolts are defined as being 2-3 orders of magnitude brighter than typical lightning, this scenario may allow normal lightning to contribute significantly to the sample of superbolts recorded from space by optical instruments. This is not the only scenario where a superbolt can arise (particularly powerful lightning sources embedded in the cloud layer can achieve similarly-bright radiances) but it confirms our explanation of "anvil superbolts" that are exceptionally bright while primarily illuminating cloud regions at the edge of the thunderstorm (Peterson et al., 2020).

## 4 Conclusion

This study uses optical Monte Carlo radiative transfer simulations with complex three-dimensional cloud scenes to explain the origins of irregular lightning radiance patterns that have been observed from orbit – including "holes" in the middle of otherwise-contiguous illuminated cloud regions, lightning that wraps around storm edges or seems to occur entirely in a warm boundary cloud that is probably not electrified, and particularly-intense lightning signals from storm edges ("anvil superbolts"). We approximate the shapes of natural stormclouds by combining cylindrical and slab cloud geometries. While a purely-cylindrical cloud might approximate growing convection, tall convection with an overhanging anvil is simulated by adding a second cylinder with a greater diameter at the top layers of the cloud. Warm boundary clouds, then, are simulated by adding an infinite slab cloud to the bottom of the primary cylinder.

These clouds are illuminated by localized point sources that approximate lightning emissions, and the radiance patterns measured by an imager above the cloud are recorded. By varying the optical thickness of the clouds and moving the point source around the cloud scene, we are able to explore the dynamics of cloud illumination and identify scenarios that result in the irregular radiance patterns of interest.

We confirm that reflections off of nearby cloud faces (particularly the lower warm boundary cloud) are an important factor that determines how the radiance measured from above is distributed spatially across the scene. When the source is located below a thick storm cloud, the brightest illumination in the scene is from "shortcuts" that the optical signals can take to reach the imager without scattering through the entire cloud depth. This is important because mid-level sources reflecting off a base layer or low-level CG sources might appear to be located outside of the storm core when the primary peak directly over the source is attenuated, reducing

534 location accuracy. Moreover, particularly thick clouds almost entirely attenuate this peak,
535 resulting in the "hole" features noted in observations. Even though overhanging anvils are a
536 "shortcut" due to their limited optical depth compared to the full cylinder, they still extinguish
537 the signals from low-level sources and can form holes by reflecting radiance back towards the
538 Earth.

539 On the other extreme, certain viewing geometries can lead to particularly favorable
540 shortcut paths where the imager can view a source located at the edge of the storm directly
541 without significant modification by the clouds. Because the measured radiance decreases
542 exponentially in the first ~1 km of cloud between the source and sensor, the radiance from such
543 an unobstructed source is up to 5 orders of magnitude brighter than the same source viewed from
544 a different angle. Thus, a normal lightning source that is observed along this particularly
545 favorable sight line can easily be labeled as a superbolt – and this appears to be the origin of our
546 "anvil superbolts" that primarily illuminate the edges of the parent thunderstorm.

547 These results show that increasing the complexity of the cloud scene provides more
548 opportunities for complex interactions with the lightning emissions, and thus increased
549 complexity in the resulting radiance pattern measured from above the storm. However, when the
550 clouds can be represented as slab layers (for example, stratiform clouds or high-altitude sources),
551 radiance profiles can be approximated with Gaussian curves. These findings support the idea that
552 we can infer cloud structure based on how the clouds are illuminated by lightning (i..e., how the
553 radiance pattern diverges from an idealized state).

554

## Acknowledgments

This work was supported by the US Department of Energy through the Los Alamos National Laboratory (LANL) Laboratory Directed Research and Development (LDRD) program under project number 20200529ECR. Los Alamos National Laboratory is operated by Triad National Security, LLC, for the National Nuclear Security Administration of U.S. Department of Energy (Contract No. 89233218CNA000001). The MCARaTS model used in this study may be acquired from its website (https://sites.google.com/site/mcarats/home), while the cloud models that serve as input data are located at Peterson (2020).

## References

Brunner K., & P. M. Bitzer ( 2020). A first look at cloud inhomogeneity and its effect on lightning optical emission. *Geophysical Research Letters*, 47, e2020GL087094. https://doi.org/10.1029/2020GL087094

Bohren, C. F., and D. R. Huffman (1983): Absorption and scattering by a sphere. In *Absorption and Scattering of Light by Small Particles*, pp.82-129, John Wiley, New York.

Christian, H.J. and S.J. Goodman, 1987: Optical Observations of Lightning from a High-Altitude Airplane. *J. Atmos. Oceanic Technol.,* **4**, 701–711, https://doi.org/10.1175/1520-0426(1987)004<0701:OOOLFA>2.0.CO;2

Christian, H. J., R. J. Blakeslee, S. J. Goodman, and D. M. Mach (Eds.), 2000: Algorithm Theoretical Basis Document (ATBD) for the Lightning Imaging Sensor (LIS), NASA/Marshall Space Flight Center, Alabama. (Available as http://eospso.gsfc.nasa.gov/atbd/listables.html, posted 1 Feb. 2000)

Goodman, S. J., R. J. Blakeslee, W. J. Koshak, D. Mach, J. Bailey, D. Buechler, L. Carey, C. Schultz, M. Bateman, E. McCaul Jr., and G. Stano, 2013: The GOES-R geostationary lightning mapper (GLM). *J. Atmos. Res.,* **125-126**, 34-49

Guo, C., and Krider, E. P. ( 1982), The optical and radiation field signatures produced by lightning return strokes, *J. Geophys. Res.*, 87( C11), 8913– 8922, doi:10.1029/JC087iC11p08913.

Iwabuchi, H., 2006: Efficient Monte Carlo methods for radiative transfer modeling. *J. Atmos. Sci.*, **63**, 2324-2339.

Iwabuchi, H., and R. Okamura, 2017: Multispectral Monte Carlo radiative transfer simulation by using the maximum cross-section method. *Journal of Quantitative Spectroscopy and Radiative Transfer*, 193, 40–46, . doi: 10.1016/j.jqsrt.2017.01.025

Light, T. E., Suszcynsky, D. M., and Jacobson, A. R. ( 2001a), Coincident radio frequency and optical emissions from lightning, observed with the FORTE satellite, *J. Geophys. Res.*, 106( D22), 28223– 28231, doi:10.1029/2001JD000727.

Light, T. E., Suszcynsky, D. M., Kirkland, M. W., and Jacobson, A. R. ( 2001b), Simulations of

lightning optical waveforms as seen through clouds by satellites, *J. Geophys. Res.*, 106( D15), 17103– 17114, doi:10.1029/2001JD900051.

Peterson, M., (2020): Cloud Models used in Lightning Radiative Transfer Simulations. https://doi.org/10.7910/DVN/0RU44I, Harvard Dataverse, DRAFT VERSION

Peterson, M., and Liu, C. ( 2013), Characteristics of lightning flashes with exceptional illuminated areas, durations, and optical powers and surrounding storm properties in the tropics and inner subtropics, *J. Geophys. Res. Atmos.*, 118, 11,727– 11,740, doi:10.1002/jgrd.50715.

Peterson, M., Rudlosky, S., & Deierling, W. ( 2017a). The evolution and structure of extreme optical lightning flashes. *Journal of Geophysical Research: Atmospheres*, 122, 13,370–13,386. https://doi.org/10.1002/2017JD026855

Peterson, M., Rudlosky, S., & Zhang, D. ( 2020). Changes to the appearance of optical lightning flashes observed from space according to thunderstorm organization and structure. *Journal of Geophysical Research: Atmospheres*, 125, e2019JD031087. https://doi.org/10.1029/2019JD031087

Platt, C.M., 1997: A Parameterization of the Visible Extinction Coefficient of Ice Clouds in Terms of the Ice/Water Content. *J. Atmos. Sci.,* **54**, 2083–2098, https://doi.org/10.1175/1520-0469(1997)054<2083:APOTVE>2.0.CO;2

Rudlosky, S. D., S. J. Goodman, K. S. Virts, and E. C. Bruning, 2018: Initial geostationary lightning mapper observations. *Geophys. Res. Lett.*, **46**, 1097– 1104. https://doi.org/10.1029/2018GL081052

Stephens, G. L., G. W. Paltridge, and C. M. R. Platt, 1978: Radiation profiles in extended water clouds, III. Observations. *J. Atmos. Sci.,* **35,**2133–2141.

Suszcynsky, D. M., Kirkland, M. W., Jacobson, A. R., Franz, R. C., Knox, S. O., Guillen, J. L. L., and Green, J. L. ( 2000), FORTE observations of simultaneous VHF and optical emissions from lightning: Basic phenomenology, *J. Geophys. Res.*, 105( D2), 2191–2201, doi:10.1029/1999JD900993.

Thomas, R., P.R. Krehbiel, W. Rison, T. Hamlin, D. J. Boccippio, S. J. Goodman, and H. J. Christian, 2000: Comparison of ground-based 3-dimensional lightning mapping observations with satellite-based LIS observations in Oklahoma. *Geophys. Res. Lett.*, **27**, 12, 1,703-1,706.

Thomson, L.W. and E.P. Krider, 1982: The Effects of Clouds on the Light Produced by Lightning. *J. Atmos. Sci.,* **39**, 2051–2065, https://doi.org/10.1175/1520-0469(1982)039<2051:TEOCOT>2.0.CO;2

Turman, B. N. ( 1977), Detection of lightning superbolts, *J. Geophys. Res.*, 82( 18), 2566– 2568, doi:10.1029/JC082i018p02566.

van de Hulst, H. C. (1980). Multiple Light Scattering, vols. 1 and 2, Academic, San Diego, Calif.

637
638
639
640

LA-UR 20-23479

641 **Table 1.** Inputs into the MCARaTS model that define the point source, atmospheric model, and
642 optical imager.
643

| | Nominal Value | | Resolution / Delta | |
|---|---|---|---|---|
| Configuration Parameter | Clear Air | Cloud | Clear Air | Cloud |
| POINT SOURCE: | | | | |
| Power | 1e9 W | | ----- | |
| Wavelength | 6670 nm | | Monochromatic | |
| ATMOSPHERIC MODEL: | | | | |
| 1-D Vertical Layers | 47 layers from 0 – 30 km | | 250 m [0-10 km], 1 km [10-15 km], 10 km [10-30 km] | |
| 3-D Vertical Layers | 21 layers starting at 500 m altitude | | 250 m | |
| 3-D Horizontal Grid | 60 x 60 square grid with infinite horizontal repetition | | 100-200 m | |
| Phase Function | Foreword transport only | Henyey-Greenstein Mie scattering approximation | 1° per angle bin | |
| Asymmetry Factor (g) | ----- | 0.84 | ----- | ----- |
| Single-Scattering Albedo ($\bar{\omega}_o$) | ----- | 0.99996 | ----- | ----- |
| Extinction Coefficient | 1.e-35 $m^{-1}$ (numerical fill value) | Variable, 0.01 – 0.08 $m^{-1}$ | ----- | ----- |
| Maximum Vertical Extent | ----- | 5,250 m | ----- | ----- |
| Maximum Optical Depth | ----- | 52 – 420 | ----- | ----- |
| IMAGER: | | | | |
| Field of View Full Width | 45°, 120° | | 0.14° per pixel | |
| Altitude | 30 km | | ----- | |
| Pointing | Nadir | | ----- | |

644
645
646
647

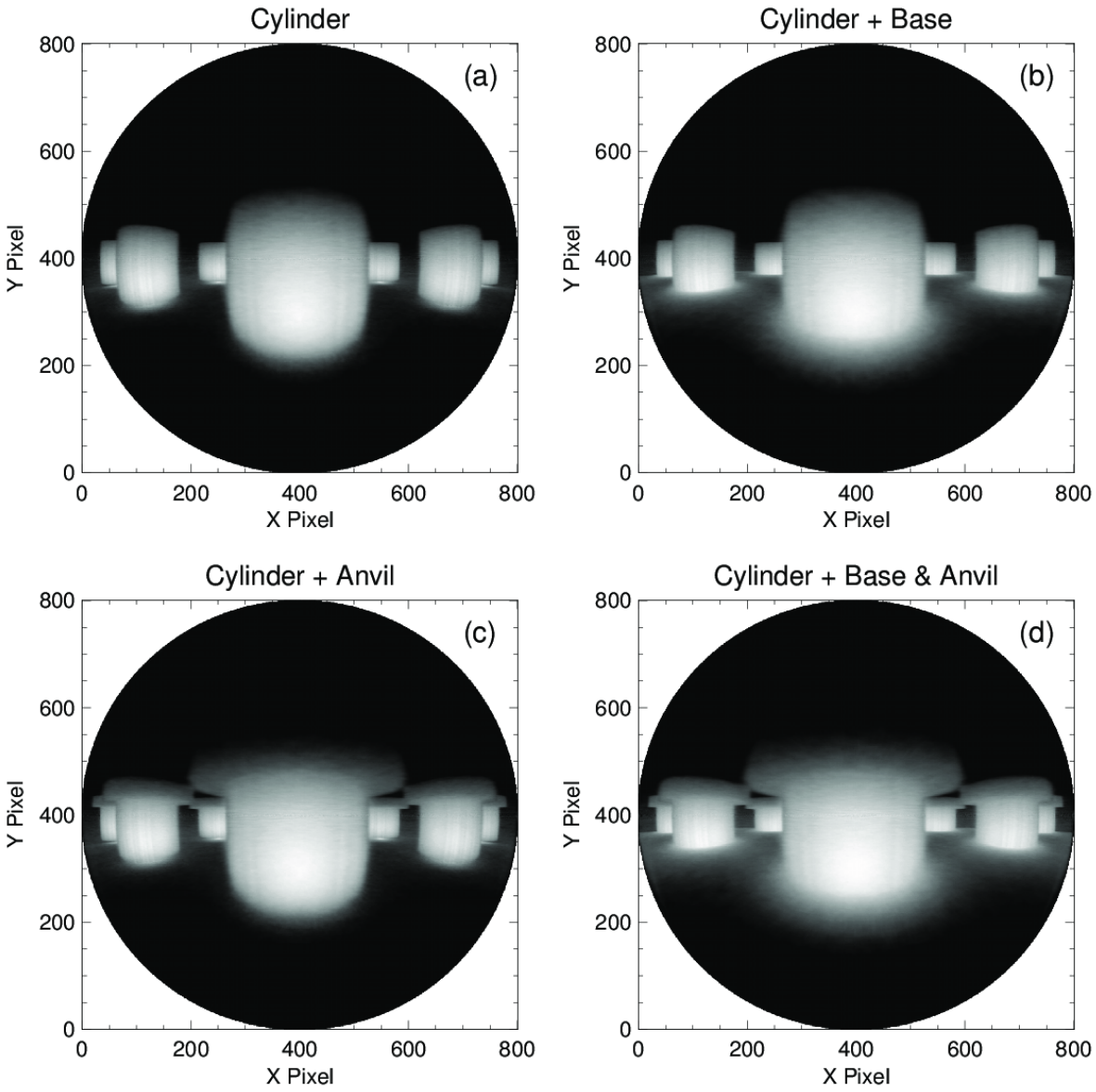


**Figure 1.** Visualization of the geometries of the finite cylindrical clouds. A wide angle (180°) camera is placed at the mid-level of the 3D cloud domain and pointed towards the horizon. The radiance from the Cylinder (a), Cylinder + Base (b), Cylinder + Anvil (c) and Cylinder + Base & Anvil illuminated from below are recorded with a logarithmic normalization.

655

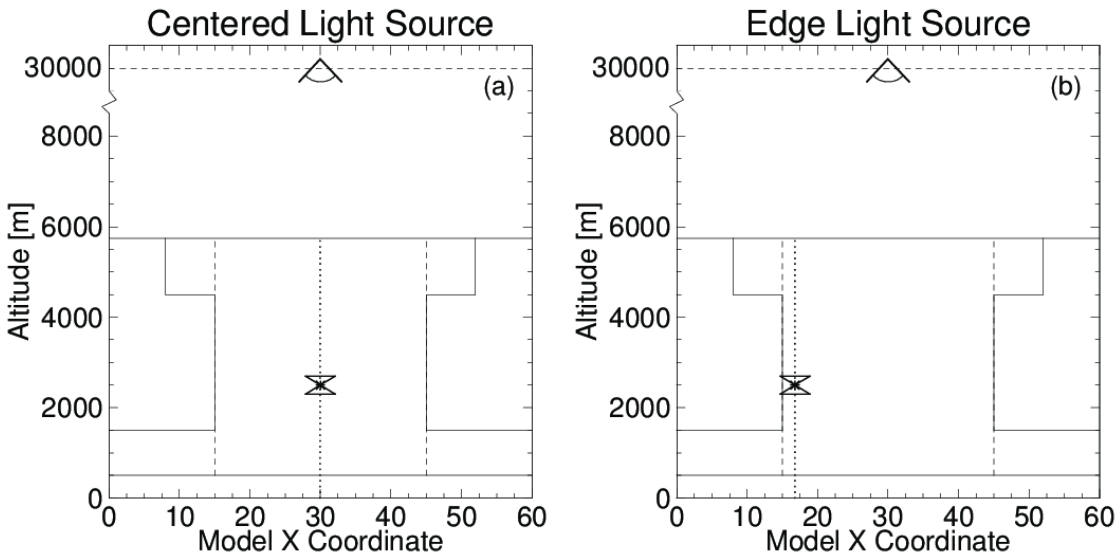


656

657 **Figure 2.** Experimental setup showing the location of the light source (double triangle) and
658 imager (eye symbol) in the cylindrical cloud geometries for (a) Scenario A where the source is at
659 the geometric center of the cloud, and (b) Scenario B where the source is located near the edge of
660 the primary cylinder. Solid lines outline the outer boundaries of the slab and most complex
661 cylindrical clouds while dashed lines show the primary cylinder radius. Dotted lines indicate the
662 range of altitudes where the light source may be positioned.

663

664

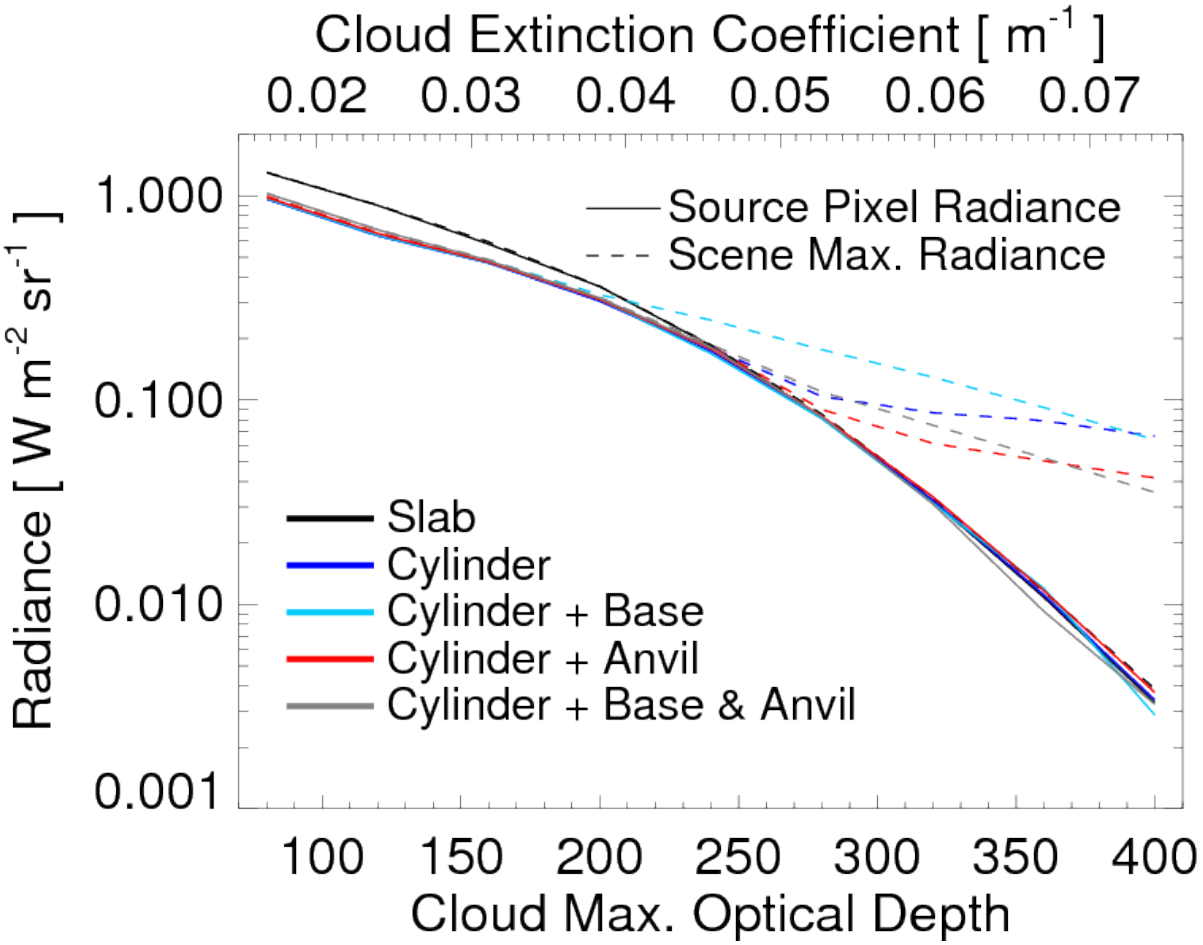


665
666
667 **Figure 3.** Source pixel (solid lines) and scene max (dashed lines) radiance from a surface-level
668 $10^9$ W source illuminating each cloud geometry (colors) with varying cloud extinction
669 coefficients and optical depths.
670

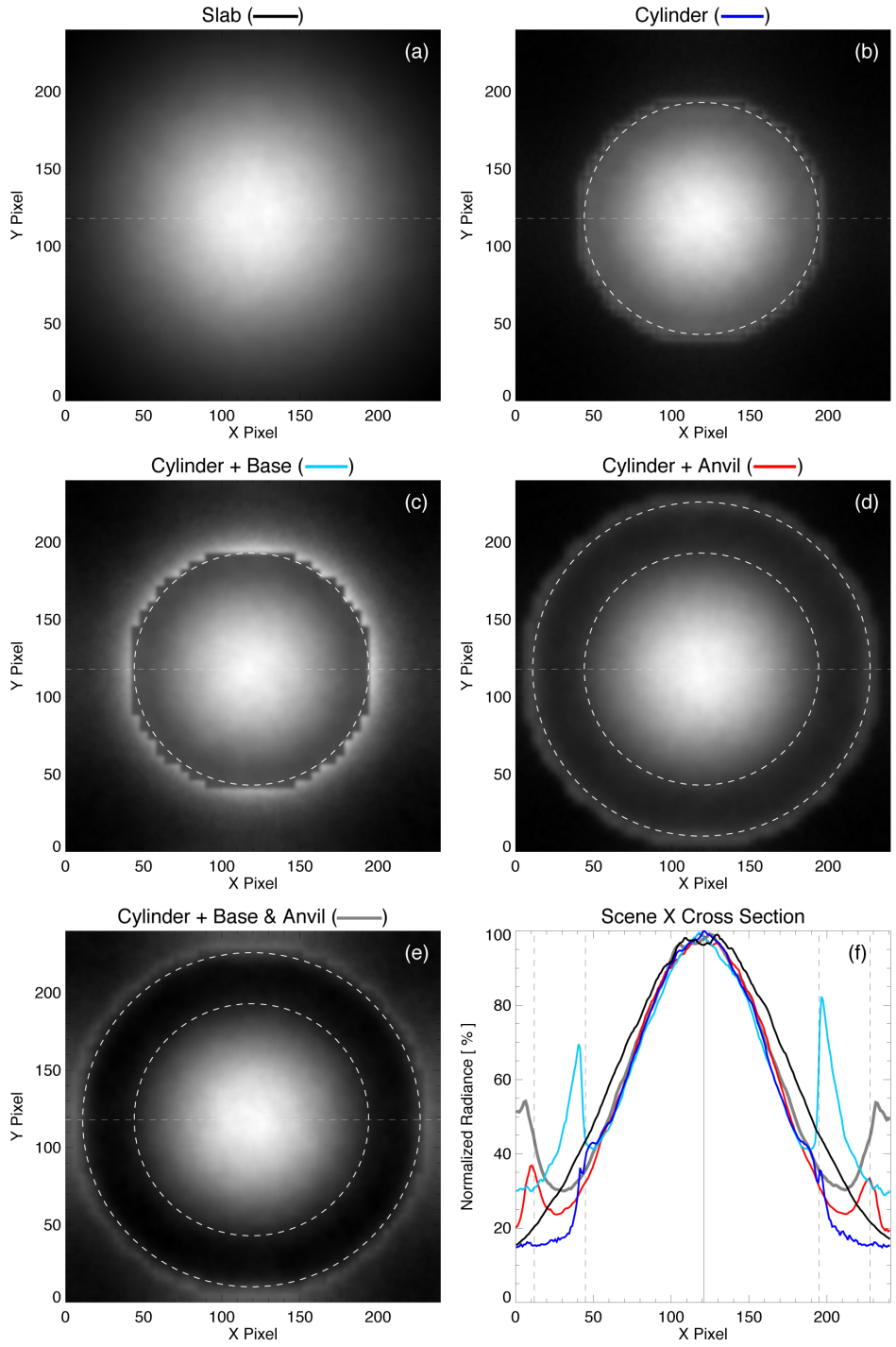


**Figure 4.** Radiance patterns from a surface-level source illuminating a Slab (a), Cylinder (b), Cylinder + Base (c), Cylinder + Anvil (d), and Cylinder + Base & Anvil (e) cloud with an overall optical depth of 160. The cloud center is indicated with an asterisk symbol. Radiance cross sections along the imager X axis (dashed lines in a-e) are shown in (f) where the colors corresponding to each cloud are indicated in the titles for a-e. Radii corresponding to the bases of the primary cylinder (inner) and anvil cloud layer (outer) are shown as dashed circles in (a-e) (where present) and dashed vertical lines in (f).

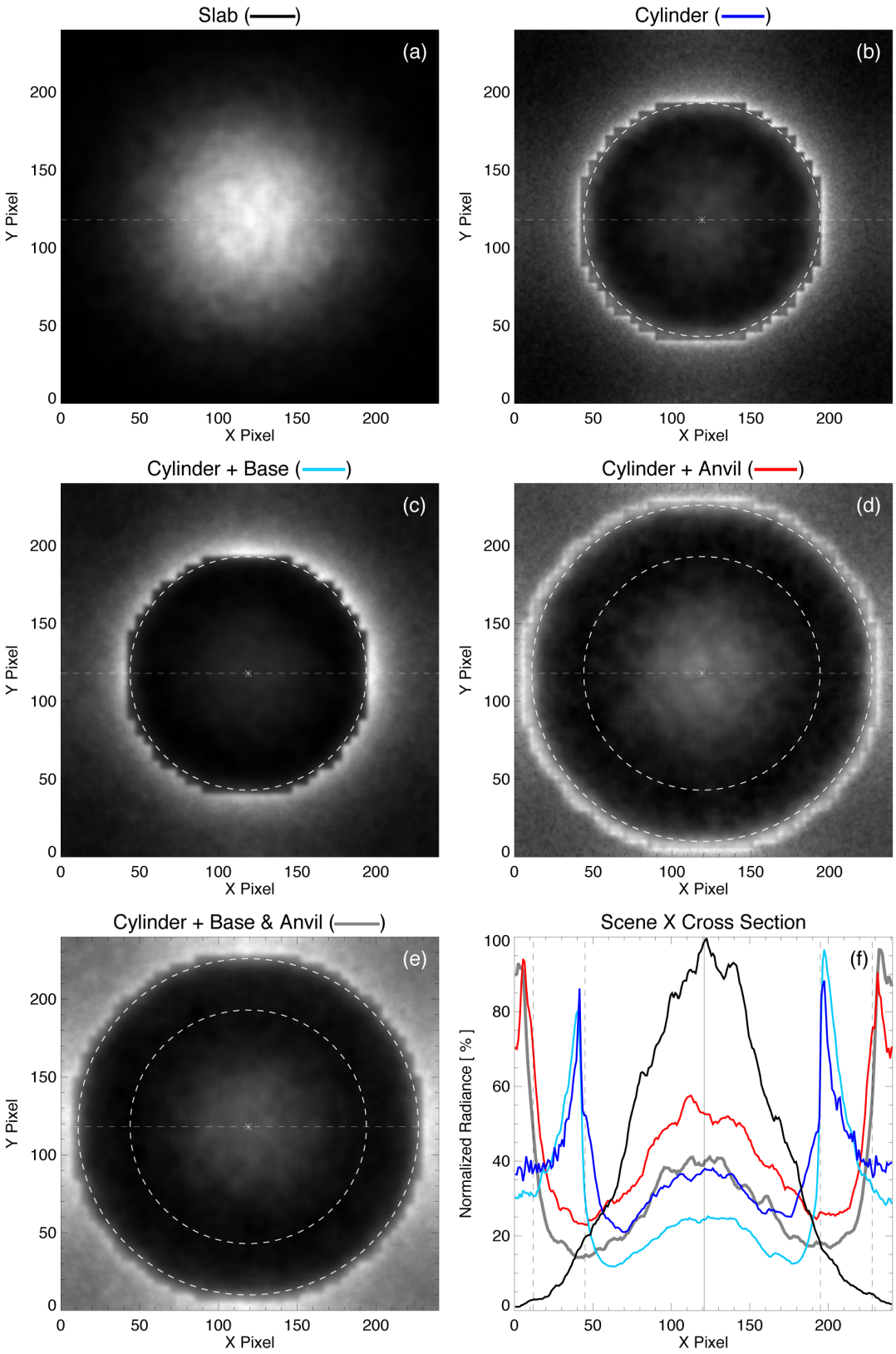


**Figure 5.** The same as Figure 4, but for the radiance patterns from a surface-level source illuminating clouds with an overall optical depth of 320.

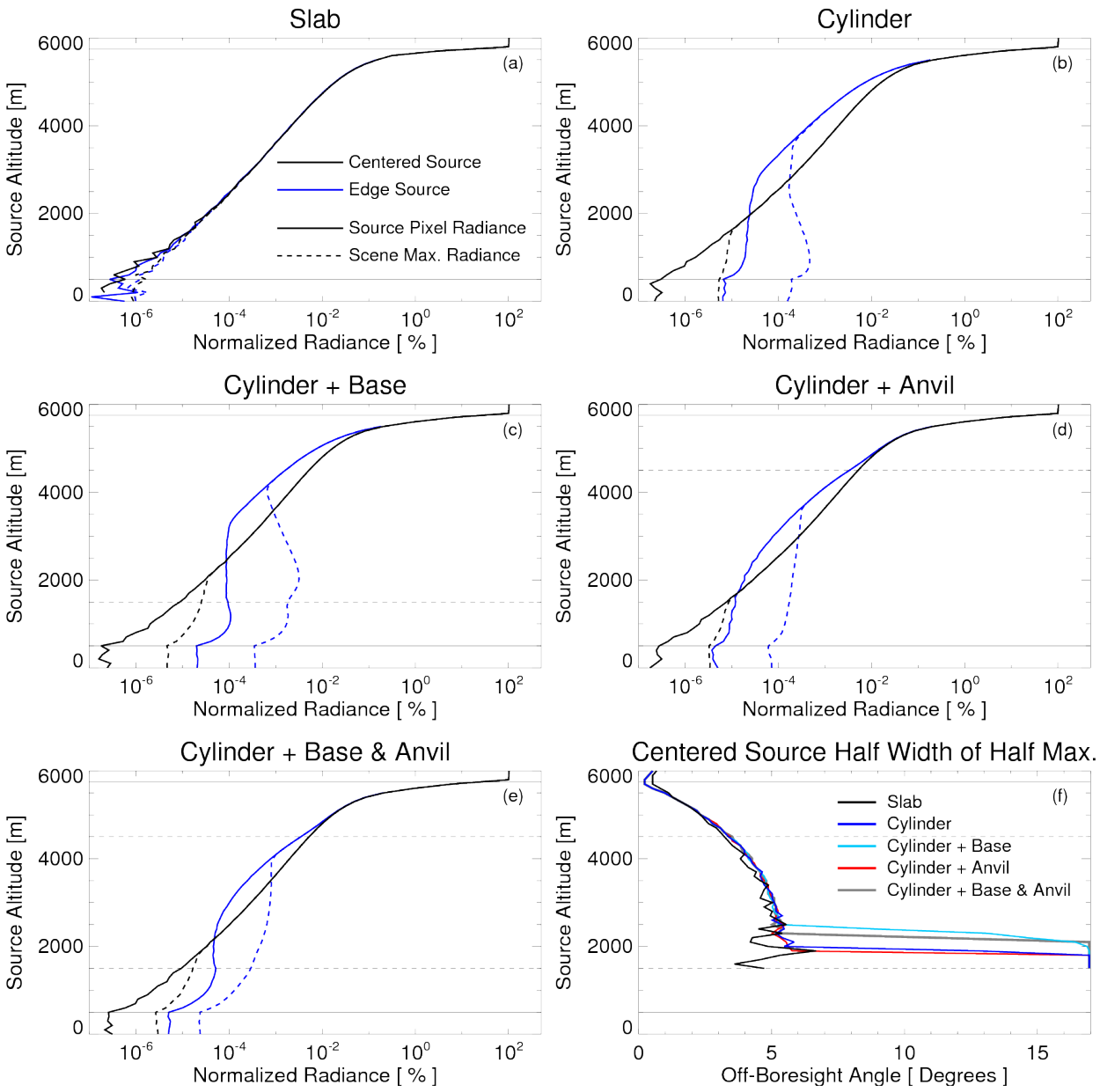


**Figure 6.** Profiles of the source pixel (solid lines) and scene max (dashed lines) radiance from centered (black) and edge (blue) sources at various altitudes illuminating Slab (a), Cylinder (b), Cylinder + Base (c), Cylinder + Anvil (d), and Cylinder + Base & Anvil (e) clouds with an overall optical depth of 400. Radiances are normalized relative to an unobstructed source at the cloud top (i.e., 100% at 5750 m). The Half Width of Half Maximum for each cloud type and source altitude above 1500 m is calculated in (f). The overall boundaries of each cloud layer are indicated with horizontal solid black lines, while the altitudes of the base layer and anvil cloud layer are indicated with dashed lines.

695

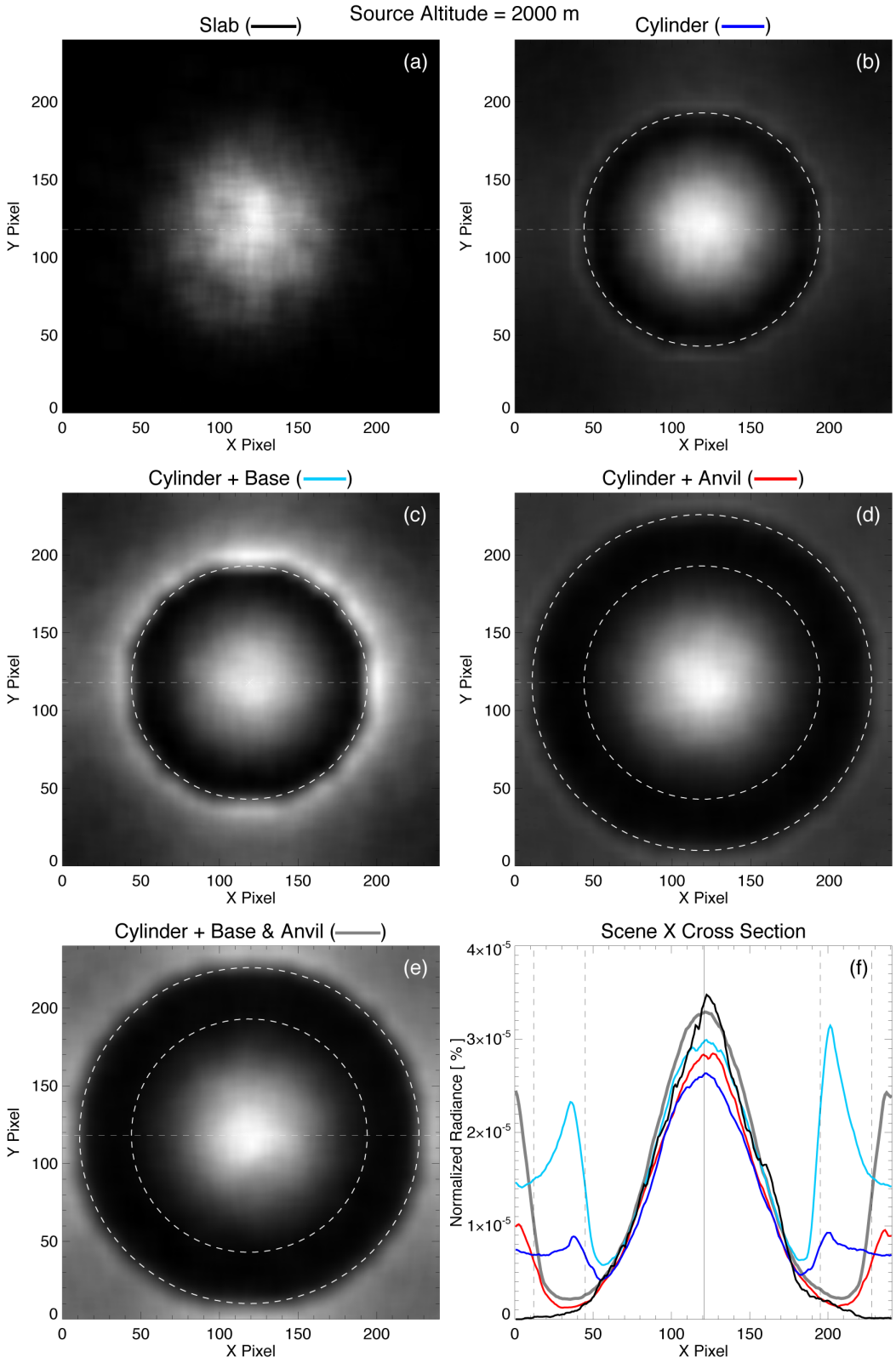


696
697 **Figure 7.** As in Figure 3, but for radiance patterns from a centered source located at 2000 m
698 altitude illuminating clouds with an overall optical depth of 400.

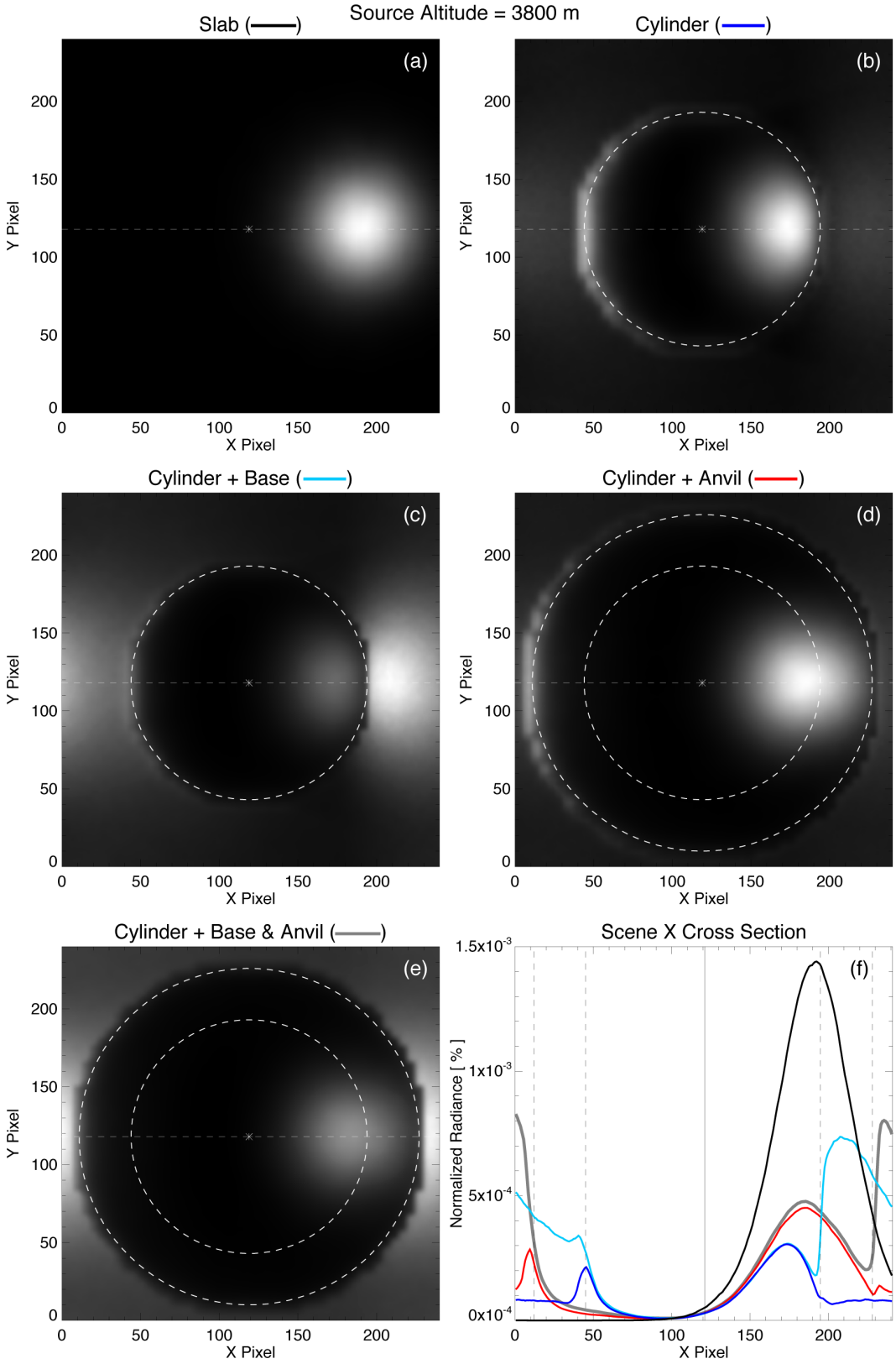


**Figure 8.** As in Figure 3, but for radiance patterns from an edge source located at 3800 m altitude illuminating clouds with an overall optical depth of 400.

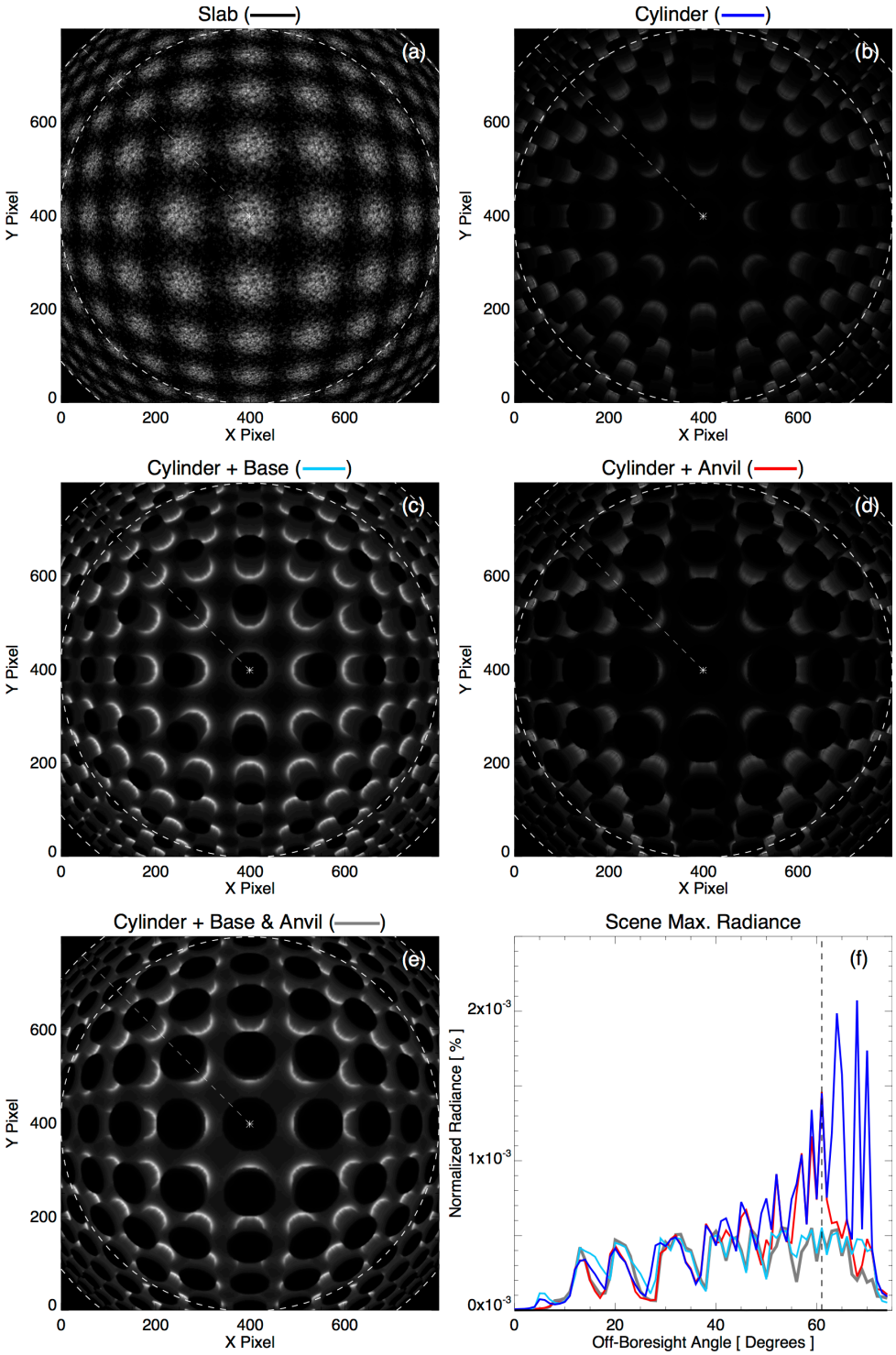


**Figure 9.** Radiance patterns (a-e) from multiple cloud tiles illuminated by centered surface-level sources (with a 100 m horizontal grid spacing) over an expanded 120° imager FOV. The radii corresponding to the nominal imager FOV (inner) and horizon (outer) are indicated with dashed circles. Radial cross sections of peak radiance (radial dashed line in a-e) for each cloud type are shown in (f) as a function of off-boresight angle. The edge of the nominal imager FOV is indicated with a dashed vertical line in (f). As in Figure 6, radiance is normalized relative to an unobscured cloud-top source.

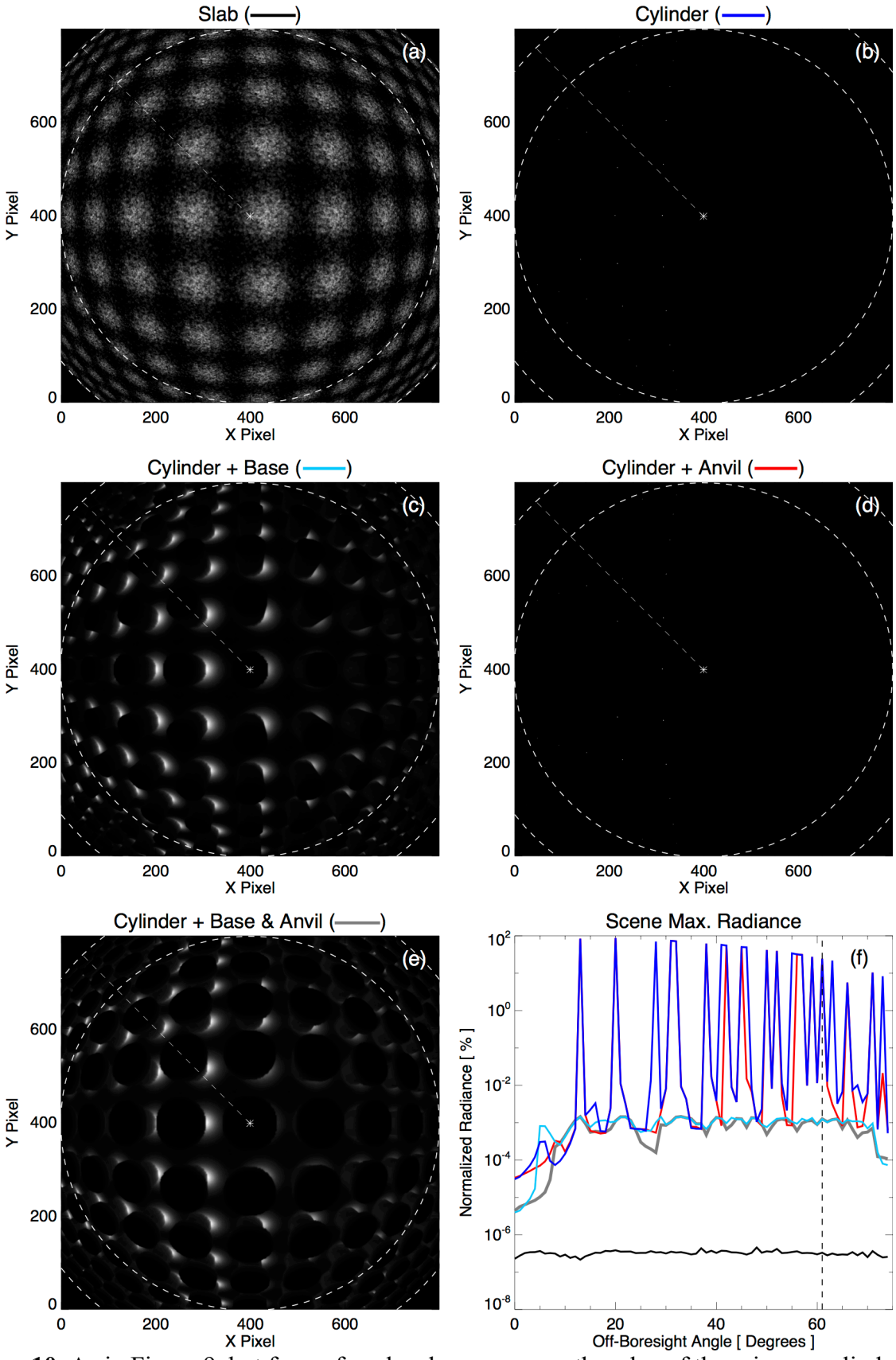


**Figure 10.** As in Figure 9, but for surface-level sources near the edge of the primary cylinder.